ENGINEERING

2016 © The Authors, some rights reserved; exclusive licensee American Association for the Advancement of Science. Distributed under a Creative Commons Attribution NonCommercial License 4.0 (CC BY-NC).
10.1126/sciadv.1601014

Mechanical assembly of complex, 3D mesostructures from releasable multilayers of advanced materials

Zheng Yan,[1]* Fan Zhang,[2]* Fei Liu,[2] Mengdi Han,[3] Dapeng Ou,[2] Yuhao Liu,[1] Qing Lin,[1] Xuelin Guo,[1] Haoran Fu,[2] Zhaoqian Xie,[4] Mingye Gao,[1] Yuming Huang,[1] JungHwan Kim,[1] Yitao Qiu,[5] Kewang Nan,[1] Jeonghyun Kim,[1] Philipp Gutruf,[1] Hongying Luo,[4,6] An Zhao,[1] Keh-Chih Hwang,[2] Yonggang Huang,[4†] Yihui Zhang,[2†] John A. Rogers[1,7†]

Capabilities for assembly of three-dimensional (3D) micro/nanostructures in advanced materials have important implications across a broad range of application areas, reaching nearly every class of microsystem technology. Approaches that rely on the controlled, compressive buckling of 2D precursors are promising because of their demonstrated compatibility with the most sophisticated planar technologies, where materials include inorganic semiconductors, polymers, metals, and various heterogeneous combinations, spanning length scales from submicrometer to centimeter dimensions. We introduce a set of fabrication techniques and design concepts that bypass certain constraints set by the underlying physics and geometrical properties of the assembly processes associated with the original versions of these methods. In particular, the use of releasable, multilayer 2D precursors provides access to complex 3D topologies, including dense architectures with nested layouts, controlled points of entanglement, and other previously unobtainable layouts. Furthermore, the simultaneous, coordinated assembly of additional structures can enhance the structural stability and drive the motion of extended features in these systems. The resulting 3D mesostructures, demonstrated in a diverse set of more than 40 different examples with feature sizes from micrometers to centimeters, offer unique possibilities in device design. A 3D spiral inductor for near-field communication represents an example where these ideas enable enhanced quality (*Q*) factors and broader working angles compared to those of conventional 2D counterparts.

INTRODUCTION

Complex, three-dimensional (3D) mesostructures are ubiquitous in biology (*1*). Man-made technologies with analogous 3D architectures could have widespread applications in biomedical devices (*2–5*), microelectromechanical systems (*6–9*), metamaterials (*10–15*), batteries (*16–21*), photonic and optoelectronic components (*22–25*), and other areas (*1*, *26*) where conventional, planar architectures currently dominate. The main challenge in realizing these systems is in the absence of fabrication/assembly methods that simultaneously provide access to 3D geometries with the necessary micro/nanoscale feature sizes and with the required classes of functional materials. For instance, techniques in 3D printing and two-photon/multiphoton lithography offer high resolution and structural versatility, but they cannot be used with device-grade semiconductors (*10*, *11*, *27–33*). Approaches that rely on strain-induced bending/folding (*34–42*) are compatible with advanced materials in conventional 2D microsystems, but the accessible range of 3D geometries is limited. Recent work demonstrates that these 2D structures can be manipulated in a conceptually different manner, via compressive buckling induced by an elastomeric support to yield broad varieties of 3D architectures characterized by open-mesh, filamentary networks (*43*, *44*), by assemblies of plates/membranes (*45*, *46*), and by various combinations. Here, 2D precursors bonded selectively at lithographically defined sites to a prestrained elastomer geometrically transform into deterministically controlled 3D architectures upon release of the prestrain. Previous work (*43–46*), however, only explored the buckling-driven assembly of 3D mesostructures from single-layer 2D precursors. The intrinsic nature of the buckling processes (for example, proportional dependence of maximum material strain on precursor thickness) in these cases constrains the range of realizable 3D mesostructures to those with open-layout geometries with largely hollow interior regions.

Here, we report the use of releasable, multilayered 2D precursors to enable the assembly of qualitatively different classes of 3D mesostructures, characterized by substantially enhanced filling factors (for example, more than three times in many examples examined herein). A set of new fabrication techniques and design concepts extend concepts in buckling-driven assembly (*44*, *45*) to allow layer-by-layer stacking of independently fabricated 2D precursors (each with different materials, feature sizes, and patterns) and separate, lithographically defined collections of bonding sites between each of these layers and the prestrained substrate. The resulting mesostructures have a level of geometric complexity unobtainable with single-layer 2D precursors reported previously. For example, specialized layouts provide local force actuators and structural supports for 3D geometries that would otherwise be impossible to achieve. Demonstrations include experimental and theoretical studies of more than 40 3D structures formed using silicon, polymer, metal, and their heterogeneous combinations, each with

[1]Department of Materials Science and Engineering and Frederick Seitz Materials Research Laboratory, University of Illinois at Urbana-Champaign, Urbana, IL 61801, USA. [2]Center for Mechanics and Materials, Applied Mechanics Laboratory, Department of Engineering Mechanics, Tsinghua University, Beijing 100084, P.R. China. [3]National Key Laboratory of Science and Technology on Micro/Nano Fabrication, Peking University, Beijing 100871, P.R. China. [4]Departments of Civil and Environmental Engineering, Mechanical Engineering and Materials Science and Engineering, Center for Engineering and Health, and Skin Disease Research Center, Northwestern University, Evanston, IL 60208, USA. [5]Department of Automotive Engineering, Tsinghua University, Beijing 100084, P.R. China. [6]School of Aerospace Engineering and Applied Mechanics, Tongji University, Shanghai 200092, P.R. China. [7]Beckman Institute for Advanced Science and Technology, University of Illinois at Urbana-Champaign, Urbana, IL 61801, USA.
*These authors contributed equally to this work.
†Corresponding author. Email: jrogers@illinois.edu (J.A.R.); yihuizhang@tsinghua.edu.cn (Y.Z.); y-huang@northwestern.edu (Yonggang Huang)

Downloaded from http://advances.sciencemag.org/ on December 5, 2016

unique levels of topological complexity and structural stability. Furthermore, an application in antennas for near-field communication (NFC) technologies demonstrates the utility of transformable, 3D geometries from releasable, multilayered 2D precursors for enhanced quality (*Q*) factor and improved working angle compared to conventional, 2D counterparts.

RESULTS

3D multilayer mesostructures with fully separated configurations

Figure 1 presents the design concepts, assembly approaches, and fabrication processes for building 3D mesostructures from releasable, multilayer, 2D precursors formed by layer-by-layer transfer printing (*47*–*49*). An illustrative example of 3D trilayer nested silicon cages appears in Fig. 1 (A and B). The process starts with the preparation of lithographically defined 2D precursors of circular cages in silicon-epoxy bilayers with three different feature sizes (radii, 1500, 1000, and 700 μm) on silicon-on-insulator (SOI) wafers (1.5 μm in thickness). Sacrificial layers (AZ 5214) patterned on top of each 2D precursor define positions of bonding sites and also allow their subsequent release from one another by transfer printing after stacking (with centers aligned). Delivery of the trilayer onto a prestrained (~70%, equal biaxial) silicone substrate followed by removal of the sacrificial layers and relaxation of the prestrain induces compressive forces that trigger independent out-of-plane buckling of each of the three 2D precursor layers to form a 3D nested cage structure. Detailed procedures appear in Materials and Methods. The initial and intermediate states of assembly obtained through finite element analyses (FEA; see the Supplementary Materials for more details) are shown in the left three frames of Fig. 1B, indicating that each layer assembles independently without any interaction between layers during the buckling process. The final configuration corresponds to nested cages, as illustrated by the results of FEA and the colorized scanning electron microscope (SEM) image (the right two frames in Fig. 1B). Note that the intermediate and final configurations denote the shapes of buckled 3D mesostructure when the prestrain is partially and completely relaxed, respectively. The color in the FEA illustrates the distribution of maximum principal strains, indicating that peak values remain well below the fracture thresholds (~2%) for the silicon.

Figure 1C presents another example, in the form of a 3D trilayer microstructure in epoxy that resembles a tree. Here, layer-by-layer transfer printing (fig. S1A) on a prestrained substrate (60%) enables the assembly; the final geometry exhibits quantitative agreement with FEA predictions (right two frames in Fig. 1C and fig. S1B). These design concepts and assembly approaches are applicable to 3D multilayer mesostructures with many different configurations. Representative examples at the microscale include bilayer saddles of epoxy (Fig. 1D), boxes of silicon (Fig. 1E), and membranes of silicon (Fig. 1F). Multilayer 2D precursors formed with different materials in different layers enable the assembly of 3D heterogeneous mesostructures. An example of a hybrid 3D trilayer nested cage appears in Fig. 1G, in which the bottom and upper layers are epoxy and the middle layer is silicon.

Mechanical/laser cutting techniques provide alternatives to photolithography for fabrication of multilayer, 2D precursors with comparatively large feature sizes (for example, from ~100 μm to several centimeters). The fabrication process is schematically illustrated in fig. S2A, and the details are provided in Materials and Methods. Highly complex 3D geometries can be achieved using these techniques, as demonstrated by two examples of Cu (1 μm)/PET (50 μm) bilayers in Fig. 1 (H and I). Figure 1H and fig. S2B present the assembly of three 2D membrane precursors into a trilayer architecture that resembles the Sydney Opera House. A variant of the tree structure in Fig. 1C, which consists of four layers and an elaborate "leaf" configuration, is illustrated in Fig. 1I and fig. S2C. The corresponding assembly process is shown in movie S1. The ribbons that connect directly to the bonding areas are ~300 μm in width, and the entire lateral size of the four-layer tree is less than 1 cm. In all of these examples, the final 3D configurations can be tailored continuously by using different levels of prestrain. The dependence of the maximum out-of-plane displacements of different layers on prestrain for three representative examples appears in fig. S3. The out-of-plane displacements of different layers all increase monotonically to approach corresponding maxima with increasing prestrain. In the various 3D architectures in Fig. 1, no evident wrinkling is observed in the contact pads that bond with the substrate, because the wrinkling wavelength for an infinitely large film (with the same thickness) compliantly bonded onto a prestretched substrate of the same material is always larger than the characteristic in-plane sizes of contact pads, typically by a factor of >2. For example, quantitative calculations based on the reported analytic models (*50*, *51*) yield wrinkling wavelengths of ~0.43, ~0.61, and ~0.61 mm for the bottom, middle, and top layers, respectively, of the nested 3D cages (Fig. 1B). These values are larger than the corresponding in-plane sizes (~0.13, ~0.2, and ~0.3 mm) of square-shaped bonding pads.

In addition to Cu/PET bilayers, these same techniques can also be applied to form 3D multilayer structures in plastic (fig. S4). As in all of the other cases, FEA predictions match experimental results.

3D multilayer mesostructures with assisting features

Each layer in the examples in Fig. 1 assembles independently, without mechanical interactions with other layers. By careful selection of the geometries of the different layers, their bonding sites, and the levels of prestrain, tailored interactions can be engineered to assist the assembly process and/or structurally stabilize the final 3D architectures. Figure 2A (top five frames) provides representative examples of interacting 3D bilayer microstructures in polyimide (PI) (green color), epoxy (yellow color), and copper/PI bilayers (orange color). The left column shows the layouts of stacked 2D precursors. Relaxing the prestrain initiates out-of-plane buckling of the base layers. Their interaction with the overlying layers imparts forces at selected locations that reshape the systems into programmed 3D configurations. The intermediate states of assembly and final configurations are given by FEA simulations and SEM images in the center and right columns of Fig. 2A, respectively. The first two examples in Fig. 2A are spire-shaped 3D bilayer mesostructures. Here, the buckled ribbon of the base layer drives the transformation of the single and double coils in the overlying layers into 3D spires. The resulting mesostructures can be used in NFC devices, as described subsequently. Moreover, both kirigami and origami design principles can be applied, as shown in the chair, box, and pyramid structures of Fig. 2A. These microstructures can be reversibly opened and closed by mechanical stretching/releasing the elastomer substrate, thereby serving as unusual types of micromanipulators (*52*). The bottom three frames of Fig. 2A correspond to 3D multilayer structures in plastic, with shapes that resemble

Downloaded from http://advances.sciencemag.org/ on December 5, 2016

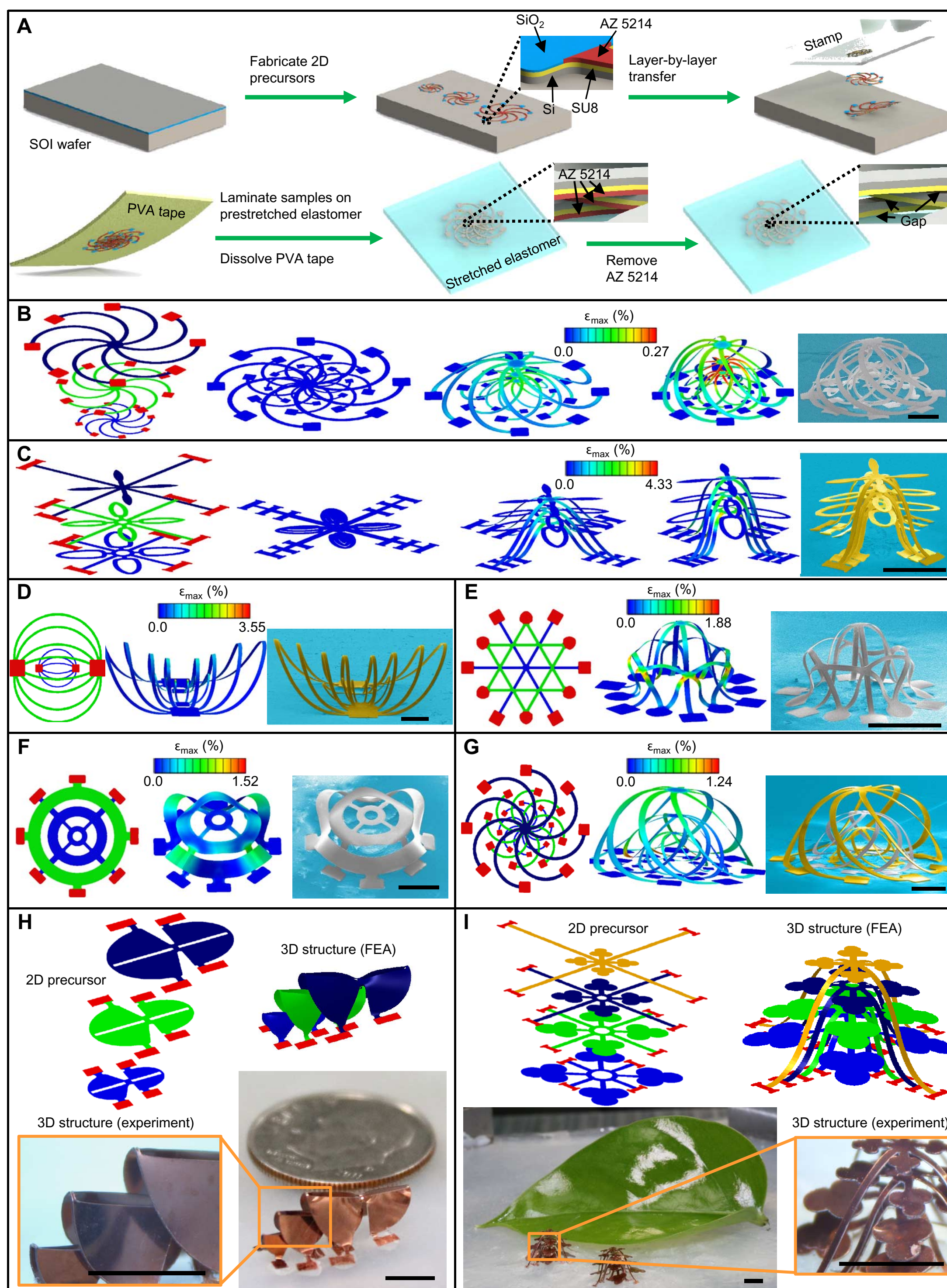

Fig. 1. Process for deterministic assembly of 3D mesostructures from releasable, multilayer, 2D precursors and illustrative examples. (**A**) Schematic illustration of the procedures for fabricating 3D multilayer mesostructures in silicon by layer-by-layer transfer printing. (**B**) Exploded view of the three precursor layers, FEA results that describe the formation of 3D trilayer nested cages in silicon, and corresponding SEM image (colorized) of the final configuration. (**C**) Similar results for a 3D trilayer microstructure in epoxy that resembles a tree. (**D** to **G**) Multilayer 2D precursors, FEA predictions for the 3D mesostructures, and corresponding SEM image for bilayer nested saddles of epoxy (D), bilayer nested boxes of silicon (E), bilayer nested membranes of silicon (F), and hybrid trilayer nested cages of epoxy and silicon (G). (**H** and **I**) Exploded view of the various precursor layers, FEA predictions for 3D mesostructures made of bilayers consisting of copper (1 μm) and polyethylene terephthalate (PET) (50 μm), and corresponding optical images for a "Sydney Opera House" (H) and a four-layer "tree" (I). The color in the FEA results of (B) to (G) corresponds to the magnitude of maximum principal strain. Scale bars, 400 μm (B to G) and 4 mm (H and I).

Downloaded from http://advances.sciencemag.org/ on December 5, 2016

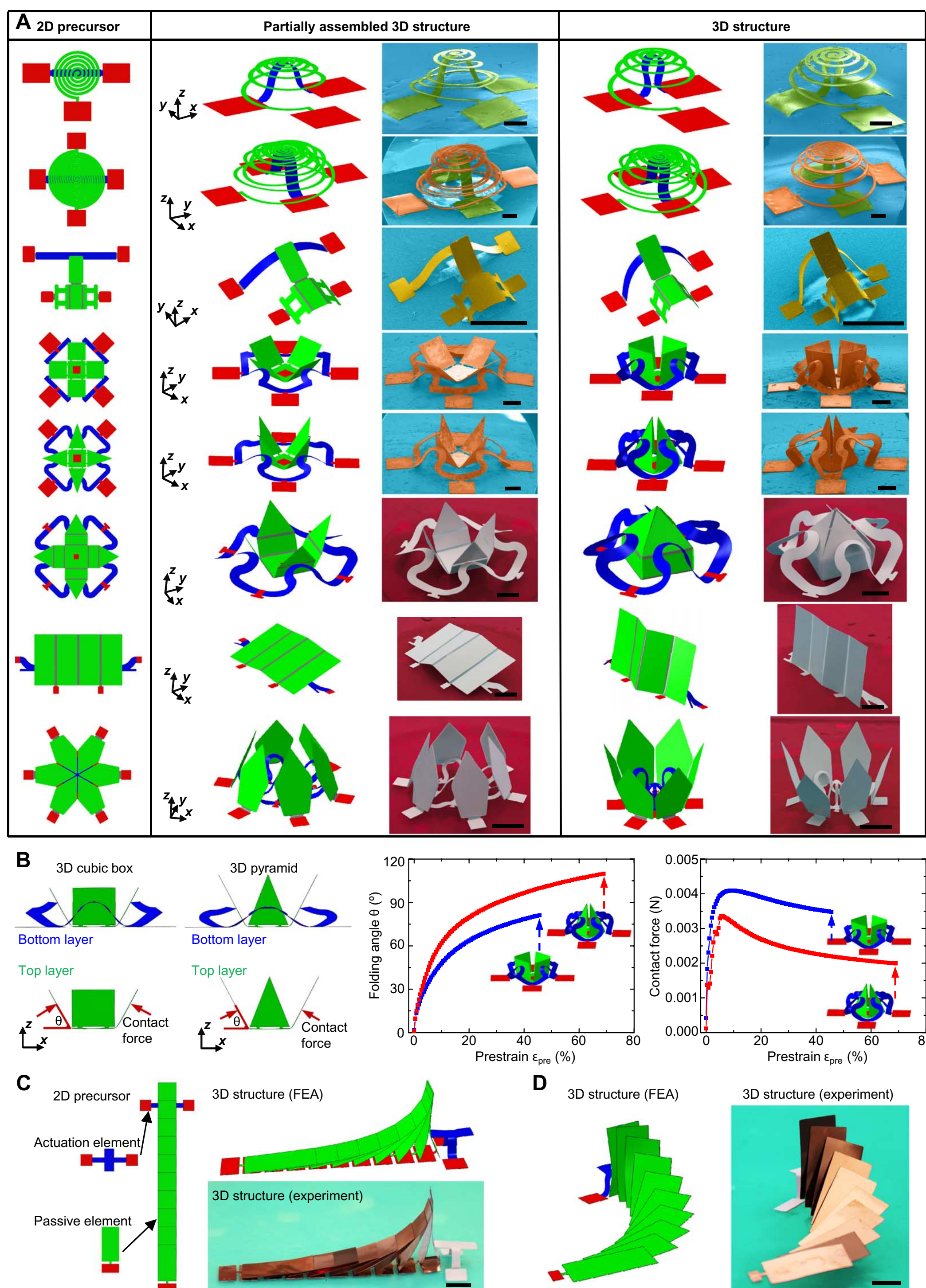

Fig. 2. Experimental and computational studies of various multilayer structures with assisting features. (**A**) Multilayer 2D precursors, FEA predictions, and experimental images (SEM or optical) of the partially and fully assembled 3D structures for eight designs formed with the use of biaxial prestrain in the substrate. The first mesostructure is made of PI (green), the second one is made of PI (green) and copper/PI bilayers (orange), the third structure is made of epoxy (SU8, yellow), the fourth and fifth mesostructures are made of copper/PI bilayers, and the last three structures are made of plastic films. The red color in the 2D precursors denotes the bonding sites, and the gray color denotes the creases with reduced thickness than the other regions. (**B**) Schematic illustration and computed results for the folding angle and normal contact force as a function of prestrain for the 3D cube and pyramid in (A). (**C**) Multilayer 2D precursors, the FEA prediction of the 3D structures made of bilayers consisting of copper (1 μm) and PET (50 μm), and the corresponding experimental image (optical) for partially collapsed arrays of Dominoes with a straight path. (**D**) Similar results for partially collapsed arrays of Dominoes with a curved path. Scale bars, 600 μm [first five structures in (A)], 20 mm [last three structures in (A)], and 5 mm (C and D).

Downloaded from http://advances.sciencemag.org/ on December 5, 2016

polyhedral boxes, screens, and blooming flowers. The "screen" structure forms through simultaneous local folding that arises from compression of the bonding sites and global rotation due to the force imparted by out-of-plane deformations of the base layer. The "blooming flower" has six petals folded by the action of the closed, circular form serpentine ribbons of the base layer. Other plastic multilayer structures that form with the precursor designs in Fig. 2A (top five frames) appear in fig. S5. The distributions of maximum principal strain in the 3D structures with evident folding deformations are illustrated in fig. S6, with magnified views to highlight the strain concentration nearby the folding creases. These results indicate that the peak values of the maximum principal strains lie well below the fracture thresholds of the materials, consistent with the experimental observations.

In all of the above examples, the mechanical interactions can be tailored quantitatively, with the aid of FEA, to precisely control the final 3D geometries. These interactions, mainly in the form of normal contact forces, act directly or indirectly (via bending moments) to reshape the overlying layers. Figure 2B and fig. S7 illustrate the dependence of the folding angle and contact force on prestrain for three representative examples. The folding angle increases monotonically with increasing prestrain, until a close geometry forms. By contrast, the contact force increases sharply and then decreases slightly with further increases in the prestrain, as the contact point moves farther away from the creases (nearby the bonding sites) at high prestrain.

Similar design concepts can be extended to form 3D shapes similar to partially collapsed arrays of Dominoes, arranged in either straight (Fig. 2C) or curved (Fig. 2D) paths. Here, a thick, crossing ribbon (plastic, ~250 μm) located at the base layer serves as the actuation element, and 10 identical pads [Cu (1 μm)/PET (50 μm) bilayer] with flexible joints connected to bonding sites serve as the passive elements for load transfer. Because of the relatively small bending stiffnesses of the joint regions, the passive elements undergo folding deformations that can be transferred sequentially to adjacent pads. Simulations indicate that the motion of the actuation element can be transferred to a relative long distance (for example, more than three times the length of a passive pad) for the design in Fig. 2C. For both straight and curved transmission paths, the multilayer configurations predicted by FEA agree with experiments, as shown in Fig. 2 (C and D) and fig. S8.

3D multilayer mesostructures with entanglements

Another class of multilayer design involves interwoven multilayers as the 2D precursors, thereby opening access to 3D mesostructures with entangled topologies. These designs can be implemented using photolithographic means or with the mechanical/laser cutting techniques mentioned previously. A schematic illustration of the process that uses mechanical cutting appears in Fig. 3A and fig. S9A, in which the interwoven regions are realized by micromanipulation. In this design, the layer in green lies above the layer in blue at the center region but below it in all of the other contacting areas. The resulting 3D mesostructures follow from collective buckling of the two entangled ribbons. The final configuration resembles a twisted knot, as shown by the FEA results and SEM images in Fig. 3B. Figure 3C and fig. S9B illustrate a ribbon network, where the green layer splits the buckled waves into two subwaves. These structures could be interesting as scaffolds for electrically or mechanically monitoring and/or stimulating the growth of cells. Figure 3D and fig. S9C demonstrate the use of an interwoven Kagome pattern consisting of two identical triangles as the 2D precursors. The final configuration has sixfold symmetry and corresponds to entangled, wavy arcs connected in a closed form. More sophisticated arrangements of the interwoven layouts can involve kirigami membranes with strategically designed cuts to serve as stitches for interweaving ribbon-shaped precursors. An example of a 3D kirigami cube with two interwoven ribbons appears in Fig. 3E and fig. S9D. These multilayer configurations might, for example, provide electromagnetic shielding for circuits formed inside the box.

3D mesostructures with coherently coupled multilayers via selective bonding

In the aforementioned designs, the 2D precursor layers involve negligible (Fig. 1) or specifically engineered (Figs. 2 and 3) mechanical interactions between one another but without any interlayer bonding. Introduction of such bonding at defined locations can further expand the design possibilities, as schematically illustrated in Fig. 4A. With multilayer 2D precursors consisting of parallel straight ribbons as an example, selective bonding enables a rich range of 3D topologies beyond those (fig. S10) possible without such bonding. For the case of uniaxial prestrain, examples appear in Fig. 4B and fig. S11 for structures in copper/PET bilayers, plastic, and hybrid combinations. The first and second columns (Fig. 4B) depict the multilayer 2D precursors in top and cross-sectional views. The red areas highlight locations of bonding either to the substrate or between layers. Corresponding 3D FEA predictions and experimental results appear in the last two columns. The first design consists of three precursor layers, in which the blue, green, and dark blue layers have two, one, and zero ends bonded to the substrate, respectively. The resulting 3D structure is distinct from that assembled from precursors without bonding. In the next two designs, each precursor layer bonds to the substrate at least at one end, thereby leading to 3D mesostructures with limited out-of-plane displacements. The last three examples in Fig. 4B demonstrate that large out-of-plane displacements can be realized by arranging the different precursor layers in a manner similar to that of building toy blocks. In particular, the multilayer structure in the fourth frame of Fig. 4B involves ribbons that increase in length from the bottom layer to the top. These structures, when constructed from piezoelectric materials, might be relevant for broadband mechanical energy harvesting.

Similar ideas implemented with biaxially prestrained substrates provide further enhanced design flexibility, as demonstrated in Fig. 4C and fig. S12. The first example corresponds to a variant of the third case in Fig. 4B, reorganized in a closed circular form. This copper/PET 3D structure consists of 15 curvy ribbons. The corresponding 2D precursors appear in fig. S12A. Adding more layers to this 3D structure along the out-of-plane direction is also possible with appropriate choice of the precursor layouts, as shown in fig. S12B and the second structure of Fig. 4C. The last three examples in Fig. 4C illustrate 3D structures supported by buckled membranes, whose 2D precursors are in fig. S12 (C to E). The third and fourth structures adopt the same 2×2 array of kirigami circular membranes at the base layer, in which the serpentine-shaped cuts induce rotational motions during the buckling process (*45*). Introducing hybrid ribbon-membrane patterns at the top layer leads to the formation of a twisted table or unfolded pads from the top of buckled kirigami membranes. The last structure in Fig. 4C is composed of cubic boxes with different sizes at the base layer and a twisted kirigami membrane at the top.

Downloaded from http://advances.sciencemag.org/ on December 5, 2016

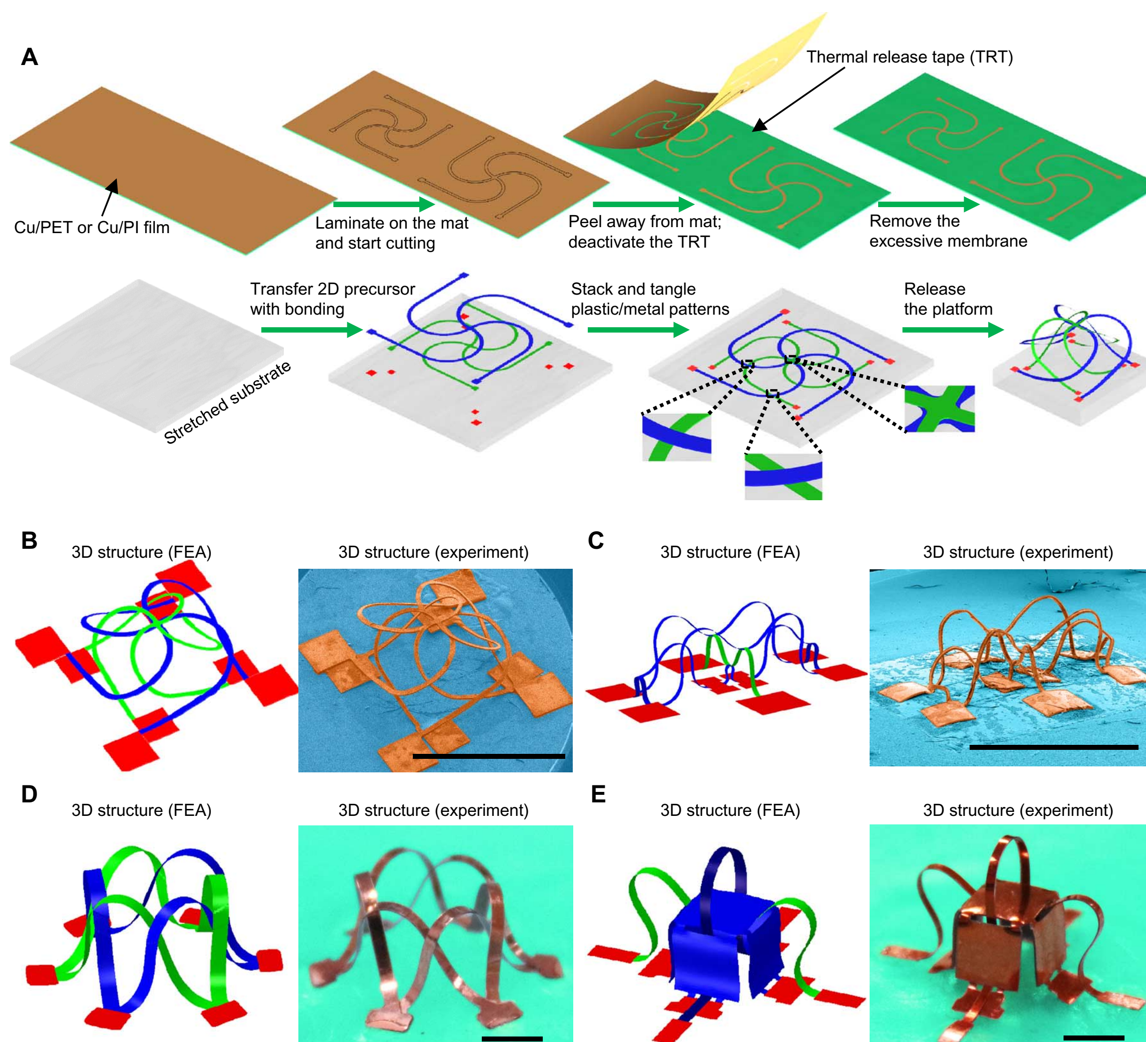

Fig. 3. Process of deterministic assembly of 3D structures from interwoven, multilayer, 2D precursors and illustrative examples. (**A**) Schematic illustration of the procedures for fabricating 3D interwoven multilayer structures of Cu/PET or Cu/PI bilayers by mechanical cutting techniques. (**B** and **C**) FEA predictions and SEM images of two multilayer mesostructures in bilayers of copper (9 μm) and PI (12 μm) with interwoven configurations. (**D** and **E**) FEA predictions and optical images of two multilayer structures in bilayers of copper (1 μm) and PET (50 μm) with interwoven configurations. Scale bars, 3 mm.

Downloaded from http://advances.sciencemag.org/ on December 5, 2016

A 3D NFC device with enhanced *Q* factor and angular operating range

The elastomeric substrate provides a straightforward means for continuous and reversible control of all of the 3D structures presented previously. This capability can be important in various applications, specifically in dynamically tunable 3D electromagnetic components. A demonstration of a mechanically tunable NFC device constructed with copper (9 μm)/PI (12 μm) bilayers, with SiO_2 encapsulation (1 μm), appears in Fig. 5. Schematic illustrations of the multilayer 2D precursors are in Fig. 5A, along with the final 3D configuration that results from the use of uniaxial prestrain ($\varepsilon_{x\text{-appl}}$ = 70% and $\varepsilon_{y\text{-appl}}$ = 0%). The geometry corresponds to a variant of the first structure in Fig. 2A but with additional turns and optimized dimensions. FEA predictions and experimental results show good agreement (right frame of Fig. 5A) for both the partially and fully assembled states. The lower-layer ribbon and upper-layer spire are electrically connected at the center of the device. Figure 5B presents measurements and modeling results for the *Q* factor and inductance at a frequency of 13.56 MHz as a function of uniaxial strain ($\varepsilon_{x\text{-appl}}$) applied to the elastomeric substrate, for two devices with different widths (w) in the supporting ribbon. Although the inductance decreases slightly during the 2D-3D transformation, the resistance decreases sharply (fig. S13A) because of a relieved "proximity effect" in the 3D configuration, thereby leading to an enhancement in the *Q* factor. This result can also be understood from the reduction in energy losses associated with decreased coupling to the supporting metallic ribbon as the separation between the two layers increases. Both experimental measurement and theoretical modeling show these enhancements (~1.5 times for w_{ribbon} = 1.03 mm and ~1.8 times for w_{ribbon} = 2 mm) of *Q* factor in 3D devices ($\varepsilon_{x\text{-appl}}$ = 0%) over 2D counterparts ($\varepsilon_{x\text{-appl}}$ = 70%), as shown in Fig. 5B. To provide further evidence of the underlying mechanism, the *Q* factors and inductances of NFC devices with a wide range of supporting ribbons widths

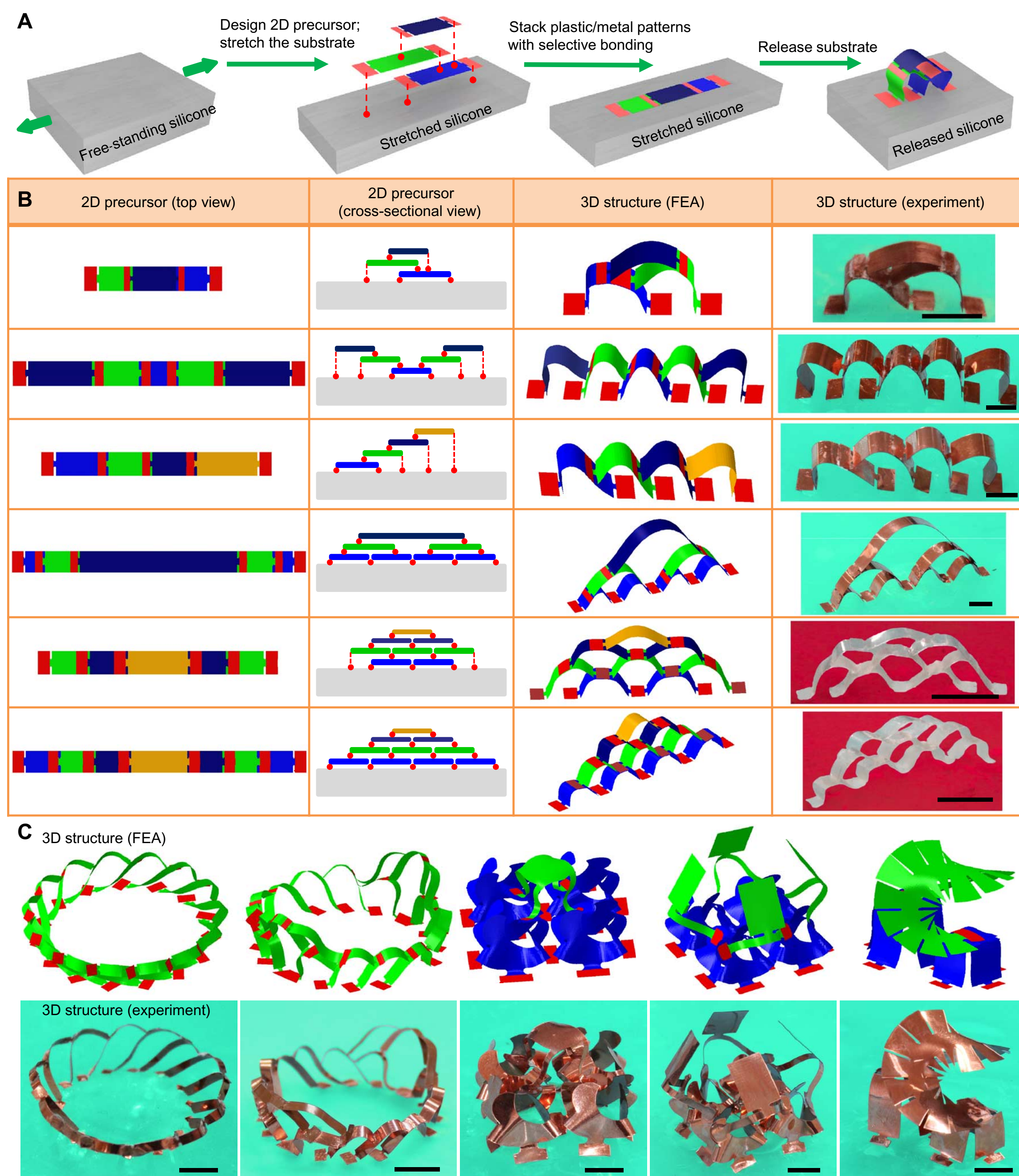

Fig. 4. Experimental and computational studies of various 3D structures with coherently coupled multilayers via selective bonding. (**A**) Schematic illustration of the assembly process of 3D structures from 2D precursors with coherently coupled multilayers that are bonded with each other at selective sites. (**B**) Multilayer 2D precursors from the top and cross-sectional views, FEA predictions, and optical images for six multilayer structures formed with the use of uniaxial prestrain in the substrate. (**C**) FEA predictions and optical images of five multilayer structures formed with the use of biaxial prestrain in the substrate. The last two structures in (B) are made of plastic films with two different thicknesses (40 μm for the bottom two layers and 25 μm for the top two layers). The other structures are all made of bilayers of copper (1 μm) and PET (50 μm), except for the second structure in (C), which consists of the same bilayers at the first floor and bilayers of copper (12 μm) and PI (12 μm) at the second floor. Scale bars, 5 mm.

Downloaded from http://advances.sciencemag.org/ on December 5, 2016

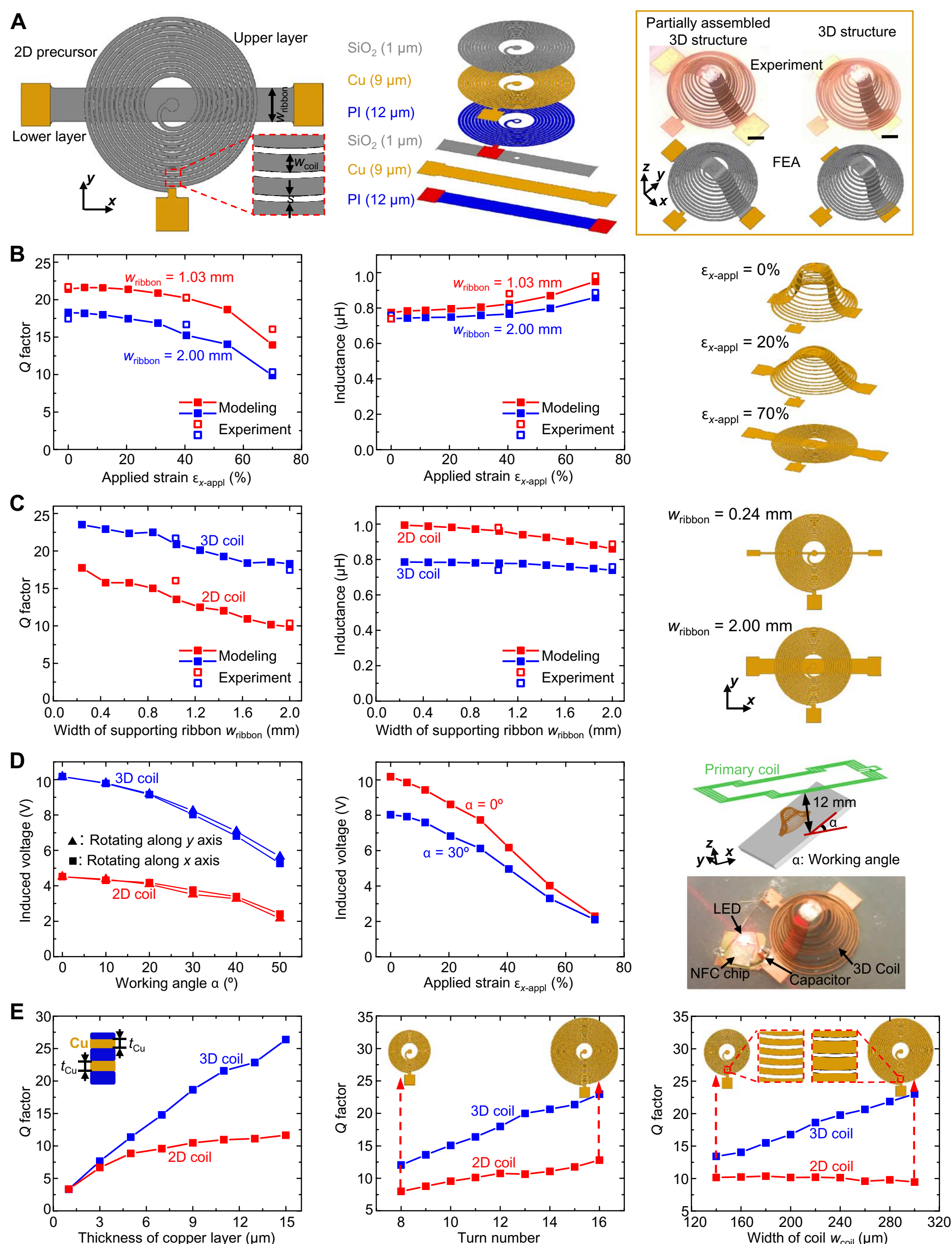

Fig. 5. A 3D NFC device with enhanced *Q* factor and improved working angle over conventional 2D counterparts. (**A**) Schematic illustration of the multilayer 2D precursors, an exploded view to show the layer construction, and the corresponding 3D configurations (optical image, right top; FEA results, right bottom) with the use of uniaxial prestrain ($\varepsilon_{x\text{-appl}} = 70\%$ and $\varepsilon_{y\text{-appl}} = 0\%$). Scale bars, 2 mm. (**B**) Measured and computed dependence of the *Q* factor and inductance on the applied strain for devices with two different widths (1.03 and 2.00 mm) in the supporting ribbon. The right frame corresponds to the FEA results of 3D configurations for the NFC device under different levels of applied strain (0, 20, and 70%). The other geometric parameters are fixed as $w_{coil} = 222$ μm (coil width), $s = 82$ μm (coil spacing), and $n_{turn} = 12$ (turn number). (**C**) Measured and computed results for the *Q* factor and inductance versus the width of supporting ribbon for both the 2D and 3D devices with $w_{coil} = 222$ μm, $s = 82$ μm, and $n_{turn} = 12$. (**D**) Computed results of the induced voltage as a function of the working angle and the applied strain, when the devices are coupled with a commercial primary coil, as schematically shown in the right top frame. A capacitor (152 pF for 2D and 182.5 pF for 3D in the left frame; 182.5 pF in the middle frame) is used for impedance matching. The right bottom frame corresponds to an optical image demonstrating the use of the 3D NFC device for lighting a commercial red LED. The geometric parameters adopted in the calculations include $w_{ribbon} = 2.00$ mm, $w_{coil} = 222$ μm, $s = 82$ μm, and $n_{turn} = 12$. (**E**) Computed *Q* factor versus the metal thickness (left, with $w_{ribbon} = 1.84$ mm, $w_{coil} = 222$ μm, $s = 84$ μm, and $n_{turn} = 12$), turn number (middle, with $w_{ribbon} = 1.84$ mm, $w_{coil} = 222$ μm, $s = 84$ μm, and $t_{cu} = 9$ μm), and the width of coil (right, with $w_{ribbon} = 1.84$ mm, $s = 84$ μm, $t_{cu} = 9$ μm, and $n_{turn} = 12$).

Downloaded from http://advances.sciencemag.org/ on December 5, 2016

(w from ~0.24 to 2 mm) appear in Fig. 5C for both 2D and 3D geometries. These results indeed show a moderate reduction in Q factor with increasing width, and these reductions are smaller in the 3D devices than in the 2D counterparts. The elastomeric substrate itself has a negligible effect on the Q factor at 13.56 MHz, as shown in fig. S13B. In an operational sense, the 3D spiral device provides an improved output voltage, when wirelessly coupled to a commercial primary coil (Samsung Galaxy Note II), after addition of a capacitor for impedance matching. Figure 5D (left frame) summarizes computed voltages for 2D and 3D devices (w_{ribbon} = 2 mm) for a range of working angles (α, from 0° to 50°). The 3D device outperforms the 2D counterpart (for example, >2.2 times) for all angles. Moreover, broad tunability of the induced voltage can be achieved for different working angles, as shown by the middle frame of Fig. 5D. The right, bottom frame of Fig. 5D and fig. S14 provides an experimental demonstration of the 3D device in lighting a commercial red light-emitting diode (LED), using the same NFC chip as in the previous studies with 2D coils (*53*, *54*).

The effects of key design parameters, including the metal thickness, turn number, and coil width, establish a comprehensive set of structure-property relationships in this system, as shown in Fig. 5E and fig. S15. These results suggest that the Q factor of the 3D spiral device increases almost in a linear manner with all of the above parameters, over the ranges of interest. The enhancement of the Q factor increases with coil width (w_{coil}), reaching ~2.4 times for w_{coil} = 300 μm. These data support broad range of tunability in Q factor via mechanical stretching.

DISCUSSION

In summary, multilayer design concepts and fabrication methods, when coupled with deterministic, substrate-induced buckling processes, open access to a wide range of 3D mesostructures, all starting with 2D precursors that can be formed using the most sophisticated materials and methods in existing microsystems technologies. Dozens of examples with length scales ranging from micrometers to centimeters, across material classes from soft polymers to brittle inorganic semiconductors, and to plastic metals, illustrate the basic ideas and validate the utility of computational modeling as a design tool. A mechanically tunable spiral NFC device provides an application example, where the 3D multilayer geometry enhances the Q factor and broadens the working angle during wireless communication with a primary coil. Quantitative analyses based on mechanical-electromagnetic modeling offer insights into the structure-property relationships of this material structure. As suggested in the main text, future additional application areas are in biomedical devices for growing and/or monitoring cells on active 3D scaffolds and in broad-frequency mechanical energy harvesters that integrate piezoelectric components in complex structures with engineered normal modes for vibration. Exploring these engineering possibilities and establishing basic considerations in accessible 3D topologies are fruitful directions for applied and fundamental research.

MATERIALS AND METHODS

Fabrication of 3D multilayer microstructures

Fabrication of 2D precursors of bilayers of silicon-epoxy and single layers of expoxy. Fabrication of 2D precursors of silicon-expoxy bilayers began with patterning the top layer of silicon on an SOI wafer (1.5-μm-thick top silicon) by photolithography and reactive ion etching. Spin-casting and photolithography then formed a layer of epoxy (SU8) on the silicon pattern in a matching geometry. Immersion in hydrofluoric acid (HF) fully removed the exposed oxide of the SOI and partially undercut this layer from the perimeter edges of the 2D silicon-epoxy structure. A coating of photoresist (AZ 5214) patterned on the top of the silicon-epoxy served as a sacrificial layer with openings to define the bonding regions. In this step, photoresist also entered the partially undercut perimeter regions to tether the silicon-epoxy bilayers and the underlying wafer. Immersion in HF fully removed the oxide to allow release of the structure from the substrate. A thin layer of silicon dioxide (SiO_2, 50 nm) blanket deposited by electron beam evaporation coated the silicon-epoxy at the positions of the openings in the photoresist and across the top surface of the photoresist as well. Immersion in acetone washed the latter SiO_2 away along with the photoresist.

Fabrication of 2D precursors of epoxy involved spin-casting and photolithography on a silicon wafer coated with SiO_2 (800 nm in thickness). The subsequent steps followed the procedures described above but with buffered oxide etchant instead of HF for partial undercut etching.

Fabrication of 2D precursors of copper-coated PI and PI. The 2D precursors of copper (9 μm)/PI (12 μm) (AC 091200EV, DuPont) and PI (12 μm in thickness) were formed by laser cutting. Deposition of SiO_2 (50 nm) by electron beam evaporation through a PI shadow mask defined the bonding sites.

Assembly of multilayer 2D precursors via layer-by-layer transfer printing. A transfer printing tool and soft, elastomeric stamps of polydimethylsiloxane (Sylgard 184, Dow Corning) enabled alignment and stacking of 2D precursors with various configurations, feature sizes, and materials. The resulting multilayer 2D precursors were delivered to the surface of a poly(vinyl alcohol) (PVA) tape.

Fabrication and assembly and interwoven 2D precursors. Fabrication began with 2D precursors of copper (9 μm)/PI (12 μm) (AC 091200EV, DuPont), interwoven manually using a micromanipulator and then delivered onto a PVA tape with the copper side down. Deposition of SiO_2 (50 nm) by electron beam evaporation through a PI shadow mask defined the bonding sites.

Buckling of 3D multilayer microstructures. A thin sheet of silicone (500 μm in thickness, Dragon Skin, Smooth-On) served as the assembly platform. Separate exposure of this substrate and the 2D precursors with ultraviolet (UV)–induced ozone radiation produced hydroxyl termination on the exposed regions of the silicone and the SiO_2. Stretching of the silicone substrate was performed with a custom stage. Lamination delivered the PVA tape onto this substrate, with 2D precursors facing downward. Baking at 70°C for 7 min promoted condensation reactions between contacting hydroxyl groups on the silicone substrates and the bonding areas of the 2D precursors, thereby creating strong mechanical interfaces at these locations. Removing the PVA tape using hot water and the AZ 5214 using acetone, followed by slow release of the prestrain in the silicone substrate while immersed in water, led to geometrical transformation of the 2D precursors into 3D microstructures.

Fabrication of millimeter-scale 3D multilayer structures

The 2D precursors in bilayers of copper (1 μm)/PET (50 μm), bilayers of copper (12 μm)/PI (12 μm), and single-layer plastic films (25, 40, 90, or 255 μm in thickness) were formed by automated mechanical cutting.

Downloaded from http://advances.sciencemag.org/ on December 5, 2016

For films thinner than 60 μm, a thermal release tape, whose adhesion reduces considerably after heating, facilitated the retrieval of the patterned films from the adhesive cutting mat, as shown in fig. S2A. Plastic films (Fig. 2A and fig. S5, C to E) with nonuniform thicknesses were prepared by mechanically cutting a base layer (90 μm in thickness) into desired patterns, followed by cutting of patterns to define the thick regions with an additional layer of thick plastic film (255 μm in thickness). Adhering the additional layers onto the base layer through thin, sticky double-coated tape (9080A, 3M) yielded 2D precursors for origami assembly.

Preparation of coherently coupled, multilayer, 2D precursors in Fig. 4 started with mechanical cutting of thin films into desired patterns. A commercial adhesive (Super Glue, Gorilla Glue Company) dispensed at desired locations on the 2D precursors resulted in strong bonding between different layers after curing for ~5 min at room temperature.

A thin silicone substrate (2 mm in thickness, Dragon Skin) served as the assembly platform. A commercial adhesive (Super Glue, Gorilla Glue Company) dispensed at desired locations on the 2D precursors resulted in strong bonding to the silicone substrate, after curing for ~10 min at room temperature. Slowly releasing the prestrain in the substrate, with a strain rate of <0.008 s^{-1}, completed the assembly process.

Fabrication and measurement of 3D NFC devices

The 3D NFC devices were formed using 2D precursors defined in copper (9 μm)/PI (12 μm) (AC 091200EV, DuPont) by laser cutting. Plasma-enhanced chemical vapor deposition through a shadow mask formed a layer of SiO_2 (1 μm) on the copper at nonbonding areas, to serve as an encapsulation layer. A transfer printing tool yielded stacked bilayer 2D precursors that were then delivered onto a piece PVA tape with the copper side facing downward. Deposition of SiO_2 (50 nm) by electron beam evaporation through a PI shadow mask defined the bonding sites, subsequently activated by exposure to UV-ozone. Removing the shadow mask and placing this tape with patterns facing downward onto prestrained elastomer substrates (Dragon Skin, Smooth-On) followed by elimination of the PVA with hot water prepared the structure for 3D assembly. A fast-drying silver paint (Electrodag 1415M, Ted Pella) connected the top layer coil and bottom layer ribbon. The 3D NFC device formed as a result of releasing the prestrain. Two electrical contact pads were connected to SubMiniature version A connectors by soldering the lead wires. The inductance and resistance of the NFC devices were characterized at 13.56 MHz using a radio-frequency impedance/material analyzer (Hewlett-Packard, 4291A).

SUPPLEMENTARY MATERIALS

Supplementary material for this article is available at http://advances.sciencemag.org/cgi/content/full/2/9/e1601014/DC1

Methods: FEA

Methods: Electromagnetic simulations

fig. S1. Experimental and FEA results of a 3D trilayer tree microstructure in epoxy.

fig. S2. Process of deterministic assembly of 3D multilayer structures using mechanical cutting techniques and illustrative examples.

fig. S3. FEA results for maximum out-of-plane displacements ($d_{\text{out-of-plane}}$) at different layers versus the prestrain in the substrate.

fig. S4. Experimental and FEA results of multilayer plastic structures with fully separated configurations.

fig. S5. Experimental and FEA results of multilayer plastic structures with assist features.

fig. S6. FEA results on the strain distributions, with magnified views near the folding creases.

fig. S7. Schematic illustration and computed results for the folding angle and normal contact force as a function of prestrain for the 3D blooming flower.

fig. S8. Illustration of the design and additional results for the partially collapsed arrays of Dominoes.

fig. S9. Designs and copper/PET structures assembled from interwoven, multilayer, 2D precursors.

fig. S10. Computational studies of fully separated mesostructures consisting of parallel straight ribbons.

fig. S11. Experimental and FEA results of plastic and plastic/metal structures with coherently coupled multilayers, assembled with use of uniaxial prestrain.

fig. S12. Experimental and FEA results of plastic structures with coherently coupled multilayers, assembled with use of biaxial prestrain.

fig. S13. Measured and computed results of resistance of the 3D spiral NFC device and the effect of substrate on the *Q* factor and inductances.

fig. S14. Circuit diagram and measured results of the 3D coil used to wirelessly power a red LED through the matching capacitor and NFC chip.

fig. S15. Computed results of inductance dependences on three key design parameters.

movie S1. Video of the assembly process guided by compressive buckling for two four-layer tree structures made of bilayers consisting of copper (1 μm) and PET (50 μm).

Downloaded from http://advances.sciencemag.org/ on December 5, 2016

REFERENCES AND NOTES

1. J. Rogers, Y. Huang, O. G. Schmidt, D. H. Gracias, Origami MEMS and NEMS. *MRS Bull.* **41**, 123–129 (2016).
2. B. Tian, J. Liu, T. Dvir, L. Jin, J. H. Tsui, Q. Qing, Z. Suo, R. Langer, D. S. Kohane, C. M. Lieber, Macroporous nanowire nanoelectronic scaffolds for synthetic tissues. *Nat. Mater.* **11**, 986–994 (2012).
3. T. G. Leong, C. L. Randallb, B. R. Bensona, N. Bassika, G. M. Sterna, D. H. Gracias, Tetherless thermobiochemically actuated microgrippers. *Proc. Natl. Acad. Sci. U.S.A.* **106**, 703–708 (2009).
4. M. R. Yu, Y. Huang, J. Ballweg, H. Shin, M. Huang, D. E. Savage, M. G. Lagally, E. W. Dent, R. H. Blick, J. C. Williams, Semiconductor nanomembrane tubes: Three-dimensional confinement for controlled neurite outgrowth. *ACS Nano* **5**, 2447–2457 (2011).
5. R. Feiner, L. Engel, S. Fleischer, M. Malki, I. Gal, A. Shapira, Y. Shacham-Diamand, T. Dvir, Engineered hybrid cardiac patches with multifunctional electronics for online monitoring and regulation of tissue function. *Nat. Mater.* **15**, 679–685 (2016).
6. D. Bishop, F. Pardo, C. Bolle, R. Giles, V. Aksyuk, Silicon micro-machines for fun and profit. *J. Low Temp. Phys.* **169**, 386–399 (2012).
7. R. J. Wood, The challenge of manufacturing between macro and micro. *Am. Sci.* **102**, 124–131 (2014).
8. W. Piyawattanametha, P. R. Patterson, D. Hah, H. Toshiyoshi, M. C. Wu, Surface- and bulk-micromachined two-dimensional scanner driven by angular vertical comb actuators. *J. Microelectromech. Syst.* **14**, 1329–1338 (2005).
9. S. Yao, Y. Zhu, Nanomaterial-enabled stretchable conductors: strategies, materials and devices. *Adv. Mater.* **27**, 1480–1511 (2015).
10. X. Zheng, H. Lee, T. H. Weisgraber, M. Shusteff, J. DeOtte, E. B. Duoss, J. D. Kuntz, M. M. Biener, Qi Ge, J. A. Jackson, S. O. Kucheyev, N. X. Fang, C. M. Spadaccini, Ultralight, ultrastiff mechanical metamaterials. *Science* **344**, 1373–1377 (2014).
11. T. A. Schaedler, A. J. Jacobsen, A. Torrents, A. E. Sorensen, J. Lian, J. R. Greer, L. Valdevit, W. B. Carter, Ultralight metallic microlattices. *Science* **334**, 962–965 (2011).
12. C. M. Soukoulis, M. Wegener, Past achievements and future challenges in the development of three-dimensional photonic metamaterials. *Nat. Photonics* **5**, 523–530 (2011).
13. J. Valentine, S. Zhang, T. Zentgraf, E. Ulin-Avila, D. A. Genov, G. Bartal, X. Zhang, Three-dimensional optical metamaterial with a negative refractive index. *Nature* **455**, 376–379 (2008).
14. J.-H. Cho, M. D. Keung, N. Verellen, L. Lagae, V. V. Moshchalkov, P. Van Dorpe, D. H. Gracias, Nanoscale origami for 3D optics. *Small* **7**, 1943–1948 (2011).
15. D. Jang, L. R. Meza, F. Greer, J. R. Greer, Fabrication and deformation of three-dimensional hollow ceramic nanostructures. *Nat. Mater.* **12**, 893–898 (2013).
16. H. Zhang, X. Yu, P. V. Braun, Three-dimensional bicontinuous ultrafast-charge and -discharge bulk battery electrodes. *Nat. Nanotechnol.* **6**, 277–281 (2011).
17. K. Sun, T.-S. Wei, B. Y. Ahn, J. Y. Seo, S. J. Dillon, J. A. Lewis, 3D printing of interdigitated Li-ion microbattery architectures. *Adv. Mater.* **25**, 4539–4543 (2013).
18. J. Deng, H. Ji, C. Yan, J. Zhang, W. Si, S. Baunack, S. Oswald, Y. Mei, O. G. Schmidt, Naturally rolled-up C/Si/C trilayer nanomembranes as stable anodes for lithium-ion batteries with remarkable cycling performance. *Angew. Chem. Int. Ed.* **52**, 2326–2330 (2013).
19. L. Pan, G. Yu, D. Zhai, H. R. Lee, W. Zhao, N. Liu, H. Wang, B. C.-K. Tee, Y. Shi, Y. Cui, Z. Bao, Hierarchical nanostructured conducting polymer hydrogel with high electrochemical activity. *Proc. Natl. Acad. Sci. U.S.A.* **109**, 9287–9292 (2012).
20. H. Wu, G. Yu, L. Pan, N. Liu, M. T. McDowell, Z. Bao, Y. Cui, Stable Li-ion battery anodes by in-situ polymerization of conducting hydrogel to conformally coat silicon nanoparticles. *Nat. Commun.* **4**, 1943 (2013).

21. X. Xiao, W. Zhou, Y. Kim, I. Ryu, M. Gu, C. Wang, G. Liu, Z. Liu, H. Gao, Regulated breathing effect of silicon negative electrode for dramatically enhanced performance of Li-ion battery. *Adv. Funct. Mater.* **25**, 1426–1433 (2015).
22. P. V. Braun, Materials chemistry in 3D templates for functional photonics. *Chem. Mater.* **26**, 277–286 (2014).
23. J.-H. Lee, C. Y. Koh, J. P. Singer, S.-J. Jeon, M. Maldovan, O. Stein, E. L. Thomas, 25th Anniversary article: Ordered polymer structures for the engineering of photons and phonons. *Adv. Mater.* **26**, 532–569 (2014).
24. M. Schumann, T. Bückmann, N. Gruhler, M. Wegener, W. Pernice, Hybrid 2D–3D optical devices for integrated optics by direct laser writing. *Light: Sci. Appl.* **3**, e175 (2014).
25. Z. Fan, H. Razavi, J.-w. Do, A. Moriwaki, O. Ergen, Y.-L. Chueh, P. W. Leu, J. C. Ho, T. Takahashi, L. A. Reichertz, S. Neale, K. Yu, M. Wu, J. W. Ager, A. Javey, Three-dimensional nanopillar-array photovoltaics on low-cost and flexible substrates. *Nat. Mater.* **8**, 648–653 (2009).
26. Y. Liu, J. Genzer, M. D. Dickey, "2D or not 2D": Shape-programming polymer sheets. *Prog. Polym. Sci.* **52**, 79–106 (2016).
27. G. M. Gratson, M. Xu, J. A. Lewis, Microperiodic structures: Direct writing of three-dimensional webs. *Nature* **428**, 386 (2004).
28. J. A. Lewis, Direct ink writing of 3D functional materials. *Adv. Funct. Mater.* **16**, 2193–2204 (2006).
29. J. A. Lewis, J. E. Smay, J. Stuecker, J. Cesarano III, Direct ink writing of three-dimensional ceramic structures. *J. Am. Ceram. Soc.* **89**, 3599–3609 (2006).
30. K. A. Arpin, A. Mihi, H. T. Johnson, A. J. Baca, J. A. Rogers, J. A. Lewis, P. V. Braun, Multidimensional architectures for functional optical devices. *Adv. Mater.* **22**, 1084–1101 (2010).
31. J. Fischer, M. Wegener, Three-dimensional optical laser lithography beyond the diffraction limit. *Laser Photonics Rev.* **7**, 22–44 (2013).
32. L. R. Meza, S. Das, J. R. Greer, Strong, lightweight, and recoverable three-dimensional ceramic nanolattices. *Science* **345**, 1322–1326 (2014).
33. C. Ladd, J.-H. So, J. Muth, M. D. Dickey, 3D printing of free standing liquid metal microstructures. *Adv. Mater.* **25**, 5081–5085 (2013).
34. V. B. Shenoy, D. H. Gracias, Self-folding thin-film materials: From nanopolyhedra to graphene origami. *MRS Bull.* **37**, 847–854 (2012).
35. V. Y. Prinz, V. A. Seleznev, A. K. Gutakovsky, A. V. Chehovskiy, V. V. Preobrazhenskii, M. A. Putyato, T. A. Gavrilova, Free-standing and overgrown InGaAs/GaAs nanotubes, nanohelices and their arrays. *Physica E: Low-dimens. Syst. Nanostruct.* **6**, 828–831 (2000).
36. O. G. Schmidt, K. Eberl, Nanotechnology: Thin solid films roll up into nanotubes. *Nature* **410**, 168 (2001).
37. M. Huang, F. Cavallo, F. Liu, M. G. Lagally, Nanomechanical architecture of semiconductor nanomembranes. *Nanoscale* **3**, 96–120 (2011).
38. T. G. Leong, A. M. Zarafshar, D. H. Gracias, Three-dimensional fabrication at small size scales. *Small* **6**, 792–806 (2010).
39. C. Py, P. Reverdy, L. Doppler, J. Bico, B. Roman, C. N. Baroud, Capillary origami: Spontaneous wrapping of a droplet with an elastic sheet. *Phys. Rev. Lett.* **98**, 156103 (2007).
40. X. Guo, H. Li, B. Y. Ahn, E. B. Duoss, K. J. Hsia, J. A. Lewis, R. G. Nuzzo, Two- and three-dimensional folding of thin film single-crystalline silicon for photovoltaic power applications. *Proc. Natl. Acad. Sci. U.S.A.* **106**, 20149–20154 (2009).
41. R. Songmuang, A. Rastelli, S. Mendach, O. G. Schmidt, SiO_x/Si radial superlattices and microtube optical ring resonators. *Appl. Phys. Lett.* **90**, 091905 (2007).
42. H. Li, X. Guo, R. G. Nuzzo, K. J. Hsia, Capillary induced self-assembly of thin foils into 3Dstructures. *J. Mech. Phys. Solids* **58**, 2033–2042 (2010).
43. Y. Sun, W. M. Choi, H. Jiang, Y. Y. Huang, J. A. Rogers, Controlled buckling of semiconductor nanoribbons for stretchable electronics. *Nat. Nanotechnol.* **1**, 201–207 (2006).
44. S. Xu, Z. Yan, K.-I. Jang, W. Huang, H. Fu, J. Kim, Z. Wei, M. Flavin, J. McCracken, R. Wang, A. Badea, Y. Liu, D. Xiao, G. Zhou, J. Lee, H. U. Chung, H. Cheng, W. Ren, A. Banks, X. Li, U. Paik, R. G. Nuzzo, Y. Huang, Y. Zhang, J. A. Rogers, Assembly of micro/nanomaterials into complex, three-dimensional architectures by compressive buckling. *Science* **347**, 154–159 (2015).
45. Y. Zhang, Z. Yan, K. Nan, D. Xiao, Y. Liu, H. Luan, H. Fu, X. Wang, Q. Yang, J. Wang, W. Ren, H. Si, F. Liu, L. Yang, H. Li, J. Wang, X. Guo, H. Luo, L. Wang, Y. Huang, J. A. Rogers, A mechanically driven form of Kirigami as a route to 3D mesostructures in micro/nanomembranes. *Proc. Natl. Acad. Sci. U.S.A.* **112**, 11757–11764 (2015).
46. Z. Yan, F. Zhang, J. Wang, F. Liu, X. Guo, K. Nan, Q. Lin, M. Gao, D. Xiao, Y. Shi, Y. Qiu, H. Luan, J. H. Kim, Y. Wang, H. Luo, M. Han, Y. Huang, Y. Zhang, J. A. Rogers, Controlled mechanical buckling for origami-inspired construction of 3D microstructures in advanced materials. *Adv. Funct. Mater.* **26**, 2629–2639 (2016).
47. A. Carlson, A. M. Bowen, Y. Huang, R. G. Nuzzo, J. A. Rogers, Transfer printing techniques for materials assembly and micro/nanodevice fabrication. *Adv. Mater.* **24**, 5284–5318 (2012).
48. M. A. Meitl, Z.-T. Zhu, V. Kumar, K. J. Lee, X. Feng, Y. Y. Huang, I. Adesida, R. G. Nuzzo, J. A. Rogers, Transfer printing by kinetic control of adhesion to an elastomeric stamp. *Nat. Mater.* **5**, 33–38 (2006).
49. S.-I. Park, Y. Xiong, R.-H. Kim, P. Elvikis, M. Meitl, D.-H. Kim, J. Wu, J. Yoon, C.-J. Yu, Z. Liu, Y. Huang, K.-c. Hwang, P. Ferreira, X. Li, K. Choquette, J. A. Rogers, Printed assemblies of inorganic light-emitting diodes for deformable and semitransparent displays. *Science* **325**, 977–981 (2009).
50. H. Jiang, D.-Y. Khang, J. Song, Y. Sun, Y. Huang, J. A. Rogers, Finite deformation mechanics in buckled thin films on compliant supports. *Proc. Natl. Acad. Sci. U.S.A.* **104**, 15607–15612 (2007).
51. Y. Zhang, S. Wang, X. Li, J. A. Fan, S. Xu, Y. M. Song, K.-J. Choi, W.-H. Yeo, W. Lee, S. N. Nazaar, B. Lu, L. Yin, K.-C. Hwang, J. A. Rogers, Y. Huang, Experimental and theoretical studies of serpentine microstructures bonded to prestrained elastomers for stretchable electronics. *Adv. Funct. Mater.* **24**, 2028–2037 (2014).
52. K. Malachowski, M. Jamal, Q. Jin, B. Polat, C. J. Morris, D. H. Gracias, Self-folding single cell grippers. *Nano Lett.* **14**, 4164–4170 (2014).
53. J. Kim, A. Banks, H. Cheng, Z. Xie, S. Xu, K.-I. Jang, J. W. Lee, Z. Liu, P. Gutruf, X. Huang, P. Wei, F. Liu, K. Li, M. Dalal, R. Ghaffari, X. Feng, Y. Huang, S. Gupta, U. Paik, J. A. Rogers, Epidermal electronics with advanced capabilities in near-field communication. *Small* **11**, 906–912 (2015).
54. J. Kim, A. Banks, Z. Xie, S. Y. Heo, P. Gutruf, J. W. Lee, S. Xu, K.-I. Jang, F. Liu, G. Brown, J. Choi, J. H. Kim, X. Feng, Y. Huang, U. Paik, J. A. Rogers, Miniaturized flexible electronic systems with wireless power and near-field communication capabilities. *Adv. Funct. Mater.* **25**, 4761–4767 (2015).

Acknowledgments: We thank J. Wang for technical support. Fabrication and measurements of microscale 3D structures were carried out at the Frederick Seitz Materials Research Laboratory, University of Illinois. Fabrication and measurements of millimeter-scale 3D structures were carried out at the Applied Mechanics Laboratory, Tsinghua University. **Funding:** J.A.R. and colleagues at the University of Illinois acknowledge the support from the U.S. Department of Energy, Office of Science, Basic Energy Sciences (award no. DE-FG02-07ER46471) for all of the work on materials, microfabrication, and assembly. Y.Z. acknowledges the support from the National Natural Science Foundation of China (grant nos. 11502129 and 11672152) and the Thousand Young Talents Program of China. Yonggang Huang and J.A.R. acknowledge the support from the NSF (grant no. CMMI-1400169) and the NIH (grant no. R01EB019337). K.-C.H. acknowledges the support from the National Basic Research Program of China (grant no. 2015CB351900). **Author contributions:** J.A.R., Y.Z., and Yonggang Huang designed and supervised the research; Z.Y. led the microscale experimental work with assistance from M.H.; F.Z. and Y.Z. led the millimeter-scale experimental work; F.Z., F.L., and Y.Z. led the structural designs, mechanics modeling, and electromagnetic modeling, with assistance from D.O., H.F., Z.X., H.L., and K.-C.H.; all other authors were involved in various aspects of the experiments; Z.Y., F.Z., Yonggang Huang, Y.Z., and J.A.R. wrote the text and designed the figures. All authors commented on the paper. **Competing interests:** The authors declare that they have no competing interests. **Data and materials availability:** All data needed to evaluate the conclusions in the paper are present in the paper and/or the Supplementary Materials. Additional data related to this paper may be requested from the authors.

Submitted 6 May 2016
Accepted 16 August 2016
Published 23 September 2016
10.1126/sciadv.1601014

Citation: Z. Yan, F. Zhang, F. Liu, M. Han, D. Ou, Y. Liu, Q. Lin, X. Guo, H. Fu, Z. Xie, M. Gao, Y. Huang, J. Kim, Y. Qiu, K. Nan, J. Kim, P. Gutruf, H. Luo, A. Zhao, K.-C. Hwang, Y. Huang, Y. Zhang, J. A. Rogers, Mechanical assembly of complex, 3D mesostructures from releasable multilayers of advanced materials. *Sci. Adv.* **2**, e1601014 (2016).

Downloaded from http://advances.sciencemag.org/ on December 5, 2016

Science Advances
AAAS

Mechanical assembly of complex, 3D mesostructures from releasable multilayers of advanced materials

Zheng Yan, Fan Zhang, Fei Liu, Mengdi Han, Dapeng Ou, Yuhao Liu, Qing Lin, Xuelin Guo, Haoran Fu, Zhaoqian Xie, Mingye Gao, Yuming Huang, JungHwan Kim, Yitao Qiu, Kewang Nan, Jeonghyun Kim, Philipp Gutruf, Hongying Luo, An Zhao, Keh-Chih Hwang, Yonggang Huang, Yihui Zhang and John A. Rogers

(September 23, 2016)
Sci Adv 2016, 2:.
doi: 10.1126/sciadv.1601014

This article is publisher under a Creative Commons license. The specific license under which this article is published is noted on the first page.

For articles published under CC BY licenses, you may freely distribute, adapt, or reuse the article, including for commercial purposes, provided you give proper attribution.

For articles published under CC BY-NC licenses, you may distribute, adapt, or reuse the article for non-commerical purposes. Commercial use requires prior permission from the American Association for the Advancement of Science (AAAS). You may request permission by clicking here.

The following resources related to this article are available online at http://advances.sciencemag.org. (This information is current as of December 5, 2016):

Updated information and services, including high-resolution figures, can be found in the online version of this article at:
http://advances.sciencemag.org/content/2/9/e1601014.full

Supporting Online Material can be found at:
http://advances.sciencemag.org/content/suppl/2016/09/19/2.9.e1601014.DC1

This article **cites 54 articles,** 10 of which you can access for free at:
http://advances.sciencemag.org/content/2/9/e1601014#BIBL

Science Advances (ISSN 2375-2548) publishes new articles weekly. The journal is published by the American Association for the Advancement of Science (AAAS), 1200 New York Avenue NW, Washington, DC 20005. Copyright is held by the Authors unless stated otherwise. AAAS is the exclusive licensee. The title Science Advances is a registered trademark of AAAS

Downloaded from http://advances.sciencemag.org/ on December 5, 2016